

Geometric dependence of critical-current variation in Al/AIO_x/Al Josephson junctions: a model-based analysis

K. Kakuyanagi,¹ N. Teran,^{1,2} H. Toida,¹ and S. Saito¹

¹*Basic Research Laboratories, NTT Inc., 3-1 Morinosato-Wakamiya, Atsugi, Kanagawa, 243-0198, Japan*

²*School of Chemistry, University of Edinburgh, David Brewster Road, Edinburgh, EH9 3FJ, Scotland, UK*

(*Electronic mail: kosuke.kakuyanagi@ntt.com)

(Dated: 1 June 2026)

Achieving uniform critical current across Josephson junctions is essential for the large-scale integration of superconducting quantum circuits. In this work, we statistically analyzed the variation of the critical current of Al/AIO_x/Al junctions using room-temperature tunnel resistance statistics, and identified the dominant contribution among the modeled sources of the variation based on their dependence on geometry and deposition conditions of junctions. Our model-based analysis reveals that fluctuations in the Al film thickness play the dominant role among the modeled contributing factors. Based on this analysis, we found that, in Dolan-bridge double-angle deposition, adopting a deposition angle of 30° for bilayer junctions significantly improves uniformity, yielding a relative standard deviation of 1.2% (0.5%) across a 9.75 mm (1.5 mm) square region.

Al/AIO_x/Al Josephson junctions fabricated by the Dolan-bridge technique¹ and Manhattan patterning^{2,3} are widely used in various quantum devices, including superconducting qubits⁴. The critical current I_C determines the Josephson energy $E_J = \Phi_0 I_C / 2\pi$ and the Josephson inductance $L_J = \Phi_0 / 2\pi I_C$; therefore, its variation directly limits circuit performance. Depending on the application, different levels of uniformity are required. For example, in transmon-based⁵ quantum processors⁶, uniformity on the order of 0.5% to 2% is required to avoid frequency collisions⁷. Similarly, high uniformity is also essential for multi-junction devices such as Josephson traveling-wave parametric amplifiers (JTWPA)^{8–10}.

To improve the uniformity of Josephson junctions, various process optimizations have been reported^{11–15}. These studies demonstrated that improved control of lithographic patterning, shadow-evaporation geometry, and oxidation conditions significantly reduces junction-area fluctuations and tunnel-barrier variations, leading to a few-percent-level dispersion in the critical current at the wafer scale. However, the microscopic mechanisms that determine the effective junction area and tunnel-barrier thickness are not yet fully understood. As a result, the fundamental origins of device-to-device variations remain unresolved.

In this work, motivated by these issues, we constructed a model of Dolan-bridge Josephson junctions based on the viewpoint that variations in the critical current arise from fluctuations in Al-film thickness, junction area, and edge roughness, each exhibiting distinct dependencies on geometry. To investigate the origins of these variations, we fabricated test junctions with systematically varied geometries and measured their room-temperature resistance. Our analysis shows that film-thickness-related fluctuations are the dominant contribution among the modeled sources of critical-current variations and provides quantitative design guidelines for improving junction uniformity in large-scale circuits.

The critical current of a superconducting tunnel junction I_C can be evaluated from the normal-state tunnel resistance R_N

using the Ambegaokar–Baratoff relation¹⁶:

$$I_C R_N = \frac{\pi \Delta}{2e} \tanh\left(\frac{\Delta}{2k_B T}\right), \quad (1)$$

where Δ is the superconducting gap, e is the elementary charge, k_B is the Boltzmann constant, and T is the temperature. Assuming that Δ is constant and the hyperbolic-tangent term approaches unity at the operating temperature of quantum devices, the product of I_C and R_N can be treated as a constant. Thus, the variation in the critical current can be related to that of the normal-state conductance $G_N = 1/R_N$. From this relationship, the variation in conductance δG_N can be expressed as

$$\delta G_N = \frac{dG_N}{dR_N} \delta R_N = -\frac{1}{R_N^2} \delta R_N. \quad (2)$$

Assuming the variations are much smaller than their average values, and from the definition of variance $\text{Var}(x) = \langle (\delta x)^2 \rangle$, we obtain the relative variances

$$\frac{\text{Var}(I_C)}{\langle I_C \rangle^2} = \frac{\text{Var}(G_N)}{\langle G_N \rangle^2} \approx \frac{\text{Var}(R_N)}{\langle R_N \rangle^2}. \quad (3)$$

Therefore, the room-temperature distribution of the normal-state resistance provides a direct estimate of the relative variations in both conductance and critical current.

To isolate short-range, intrinsic process-induced variation from long-range spatial fluctuations, we introduce the semi-variogram and its normalized form instead of relative standard deviation

$$\gamma(\mathbf{r}) = \frac{1}{2} \left\langle [R_N(\mathbf{r}_0 + \mathbf{r}) - R_N(\mathbf{r}_0)]^2 \right\rangle_{\mathbf{r}_0}, \quad (4)$$

$$\tilde{\gamma}(\mathbf{r}) = \frac{\gamma(\mathbf{r})}{\langle R_N \rangle^2}, \quad (5)$$

where \mathbf{r} is the displacement vector between two positions. It is worth noting that, under the assumption of second-order

spatial stationarity, the semivariogram can be expressed as the difference between the variance and the spatial covariance,

$$\gamma(\mathbf{r}) = \text{Var}(R_N) - \text{Cov}(R_N(\mathbf{r}_0 + \mathbf{r}), R_N(\mathbf{r}_0)). \quad (6)$$

Consequently, when spatial correlations vanish, $\gamma(\mathbf{r})$ reduces to $\text{Var}(R_N)$. By setting \mathbf{r} to the nearest-neighbor spacing of the junction array, we obtain a metric that predominantly quantifies intrinsic, process-induced variation between neighboring junctions. In the following, we refer to $\sqrt{\gamma}$ as the normalized RMS (root-mean-square) variation.

The variation of conductance is modeled as the sum of random fluctuations that are decomposed into contributions with different dependence on geometry and process parameters. In this model, we focus on intrinsic junction-to-junction variations. Long-range spatial variations, such as resist thickness undulations introduced during spin coating and smooth wafer-scale Al-thickness gradients originating from the source-to-sample distance or deposition angle, are largely suppressed by evaluating the semivariogram at the nearest-neighbor spacing. The film-thickness variation considered below therefore refers to residual local variations in the effective Al deposition geometry in the junction-forming region.

$$\delta G_N = \delta G_0 + \delta G_S(S) + \delta G_L(L) + \delta G_d(\theta, N_L, W) \quad (7)$$

Here, δG_0 denotes geometry-independent fluctuations, δG_S and δG_L represent structural fluctuations that depend on area S and edge length L , respectively, and δG_d represents fluctuations induced by film-thickness variations, with a magnitude that depends on the deposition angle θ , the number of layers N_L , and the junction width W . We assume that these fluctuation components are statistically independent, as they originate from distinct physical mechanisms and spatial scales within the fabrication process, such as lithography and deposition. The variances are modeled as follows:

$$\text{Var}(G_N) = \text{Var}(G_0) + \text{Var}(G_S) + \text{Var}(G_L) + \text{Var}(G_d), \quad (8)$$

$$\text{Var}(G_0) = c_0, \quad (9)$$

$$\text{Var}(G_S) = c_S S + c_{S^2} S^2, \quad (10)$$

$$\text{Var}(G_L) = c_L L + c_{L^2} L^2, \quad (11)$$

$$\text{Var}(G_d) = c_d f^2(\theta, N_L) W^2. \quad (12)$$

Here, the linear term in S arises from fluctuations of the oxide tunnel-barrier thickness or barrier properties that occur at a microscopic scale within the junction. The quadratic term reflects long-range spatial fluctuations that vary between junctions, such as fluctuations in the oxide tunnel-barrier thickness. Similarly for L , the linear term corresponds to short-range line-edge roughness along the junction edge, whereas the quadratic term corresponds to long-range spatial fluctuations of pattern shape and resist thickness. For the thickness-related contribution, the fluctuation in junction area induced by film-thickness variations is proportional to the junction width W , and therefore the corresponding variance scales with W^2 . The contributions associated with S and L are distinguished through their different dependences on junction geometry when the junction size is varied. The thickness-related

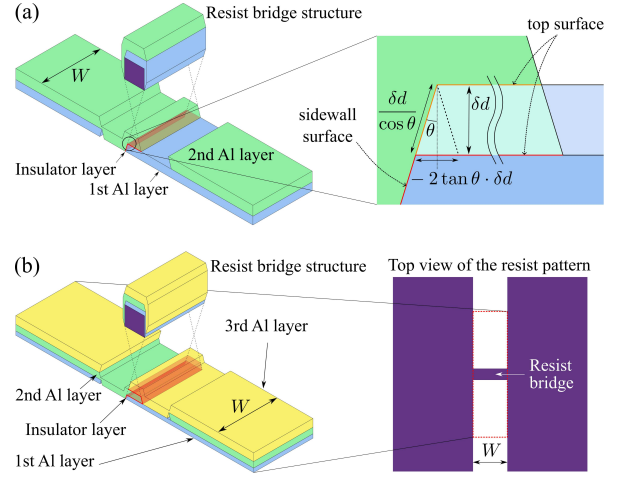


FIG. 1. (a) Cross-sectional schematic of the Al/AlO_x/Al bilayer junction formed by the Dolan-bridge (purple) double-angle deposition. The blue (green) layer represents the first (second) deposited Al film. The surfaces highlighted in red correspond to the junction interfaces with area S , and the perimeter of these surfaces corresponds to the junction-edge length L . The magnified schematic illustrates the relationship among the deposition angle θ , the film-thickness fluctuation δd , and the junction interfaces (red and orange). The sidewall surface and the top surface constitute the junction interfaces. When the film thickness increases by δd , the junction interface shifts from the line shown in red to the line shown in orange. (b) Cross-sectional schematic of the trilayer junction. The yellow layer represents the Al film deposited in the third evaporation. The right panel shows the top view of the resist pattern.

term is further separated by its dependence on the number of layers N_L through the geometric factor $f(\theta, N_L)$.

The geometric origin of the dependence on deposition angle is illustrated in Fig. 1. During angled deposition, the junction is formed both on the top and sidewall surfaces. The junction interface consists of both the top surface and the sidewall surface (Fig. 1(a)). When the film thickness changes, these two contributions change with different geometric factors, resulting in different sensitivities to film-thickness fluctuations. As a result, the contribution of film-thickness fluctuations to the critical-current variation depends on the deposition angle θ . This effect is formulated as the dimensionless geometric factor:

$$f^2(\theta, N_L) = \frac{N_L - 1}{\cos^2 \theta} \left[2N_L \sin \theta \left(\frac{2N_L - 1}{3} \sin \theta - 1 \right) + 1 \right], \quad (13)$$

whose derivation is provided in the Supplemental Material. In particular, for bilayer junctions ($N_L = 2$), the geometric factor is calculated

$$f^2(\theta, 2) = \left(\frac{1}{\cos \theta} - 2 \tan \theta \right)^2. \quad (14)$$

The origin of each term can be understood as follows. As illustrated in the magnified schematic in Fig. 1(a), an increase in film thickness increases the contribution from the sidewall surface in proportion to $1/\cos \theta$, while it decreases the contribution from the top surface in proportion to $2 \tan \theta$. This

factor vanishes at $\theta = 30^\circ$, whereas no such null angle exists for $N_L \geq 3$.

To verify the dependence of the model on geometry and process conditions, approximately 4000 Al/AlO_x/Al Josephson junctions were fabricated in a 13 mm square region of a 17 mm square Si chip by the Dolan-bridge technique¹. Si chips were coated with a 300 nm PMGI resist layer followed by a 100 nm ZEP resist layer. The designed Dolan-bridge width was 100 nm for all devices. Patterns, corrected for the proximity effect using BEAMER software (GenISys GmbH), were written by electron-beam lithography (JEOL JBX-8100FS) and developed with butyl acetate and PMGI 101A developers. The Al films were deposited using a PLASSYS MEB550S2-I UHV evaporator with deposition angles of $\pm 17^\circ$ or $\pm 30^\circ$. The thickness of the deposited Al layers ranged from approximately 10 to 70 nm. For the experiments investigating the dependence on junction geometry, the bilayer junctions had thicknesses of 40 and 50 nm, while the trilayer junctions had thicknesses of 10, 20, and 60 nm. For the experiments investigating the dependence on deposition angle, bilayer junctions were used, with layer thicknesses of 20 and 70 nm. Dynamic oxidation was performed between the depositions at an oxygen pressure of 10 mTorr for 30 min. During oxidation, the sample holder was rotated at five revolutions per minute to enhance spatial uniformity, following a fabrication procedure similar to that described in Ref. 11.

The four-terminal resistance of the junctions was measured automatically at room temperature using a probe station. Outliers deviating by more than $\pm 20\%$ from the median value were treated as open or shorted junctions and excluded from the analysis. This threshold is much larger than the intrinsic variation discussed below, and is used only to remove clearly defective junctions.

To examine the geometric dependence, we fabricated and measured test junctions with four different junction widths at deposition angles of $\pm 17^\circ$. To ensure identical process conditions, junctions with each width were fabricated in separate 6.2 mm-square regions on the same chip, each containing 1024 test junctions. Additionally, bilayer junctions and trilayer junctions, as shown in Fig. 1(b), were fabricated to evaluate the effect of the number of Al layers N_L . Note that the multilayer junction considered here does not correspond to Josephson junctions connected in series; rather, the successive deposition layers do not form electrically distinct junctions but instead contribute in parallel to a single effective junction interface with increased area.

Figure 2 shows the normalized RMS variation as a function of junction width, together with the fitting results using the model [Eq. (8)]. Here, we fit the variance of the normalized resistance variation to the model. The variance is obtained as the square of the experimentally measured normalized RMS variation, and the model describes the intrinsic process-induced variance. The combined dataset consists of eight measured values obtained by varying the junction width W and the number of deposited layers N_L , whereas the model contains six non-negative fitting coefficients. In addition, the model terms have distinct functional dependences on W and N_L , and the corresponding basis functions are linearly independent for the

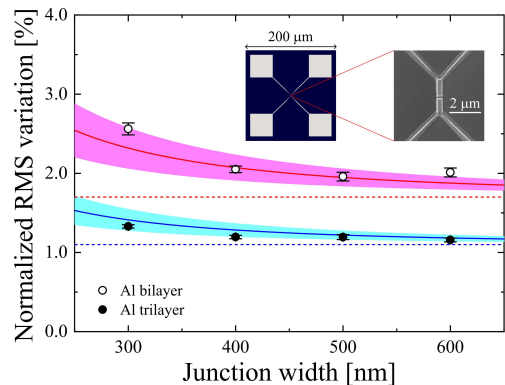


FIG. 2. Geometry dependence of the measured normalized RMS variation and the corresponding model fitting results. White (black) circles represent the measured data for the bilayer (trilayer) junctions, and the error bars are estimated from the unbiased sample variance. The red (blue) solid line represents the model fitting results for the bilayer (trilayer) junctions. The dashed horizontal lines indicate the asymptotic values of the normalized RMS variation for the bilayer and trilayer junctions, which correspond to the contribution from film-thickness fluctuations. The magenta (cyan) shaded region indicates the uncertainty of the fitted curve for the bilayer (trilayer) junctions, calculated from the standard errors of the fitting parameters. Inset (top center): pattern of the unit cell of a test junction. For four-terminal measurements, each test junction is connected to four square electrodes with a side length of $50 \mu\text{m}$. Inset (top right): a scanning electron microscope image of the test junction.

measured set of geometries. Therefore, the fitting problem is sufficiently constrained by the present dataset and yields a unique least-squares solution. The fitting parameters were determined from the geometry dependence of the data using a non-negativity-constrained least-squares fit, so that all variance components remain physically meaningful. The fitting results indicate that the geometry-independent term c_0 and the film-thickness-related term c_d constitute the dominant contributions to the total variance. In the constrained fit, the optimal solution satisfying the non-negativity constraints sets the area- and edge-related coefficients to zero, indicating that these terms are not required to explain the present dataset. The lower normalized RMS variation in trilayer junctions is consistent with the statistical averaging of film-thickness fluctuations across the layers, as the fluctuations in each layer are independent.

Table I summarizes the estimated contributions of geometry-independent and film-thickness-related terms for different junction geometries. Based on the quantitative decomposition summarized in Table I, these results clearly show that the contribution from film-thickness fluctuations $\sqrt{\text{Var}(G_d)}/G_N$ is the dominant component among the modeled sources of the variation. For the bilayer junctions deposited at 17° , the fitted film-thickness-related contribution is approximately 1.7%. Using the designed Dolan-bridge width of 100 nm and the bilayer geometric factor $f(17^\circ, 2) = 1/\cos 17^\circ - 2 \tan 17^\circ$, this value corresponds to an effective Al-thickness variation of approximately 4 nm. This value is not unrealistic as a local thickness variation in the ef-

TABLE I. Summary of the measured normalized RMS variation of the resistance, the corresponding model-fitted relative standard deviation, and the estimated contributions of the geometry-independent and film-thickness-related terms for different junction geometries. The thickness-induced terms are calculated for each N_L from the fitting curve of W dependence, thus the same values appear for the same N_L .

W (nm)	N_L	Measured $\sqrt{\gamma}$	Model $\sqrt{\text{Var}(G_N)}/G_N$	Independent $\sqrt{\text{Var}(G_0)}/G_N$	Thickness $\sqrt{\text{Var}(G_d)}/G_N$
300	2	$2.56 \pm 0.08\%$	$2.32 \pm 0.21\%$	$1.57 \pm 0.61\%$	$1.70 \pm 0.18\%$
400	2	$2.05 \pm 0.04\%$	$2.07 \pm 0.17\%$	$1.18 \pm 0.46\%$	$1.70 \pm 0.18\%$
500	2	$1.96 \pm 0.06\%$	$1.95 \pm 0.11\%$	$0.94 \pm 0.37\%$	$1.70 \pm 0.18\%$
600	2	$2.01 \pm 0.06\%$	$1.88 \pm 0.07\%$	$0.79 \pm 0.31\%$	$1.70 \pm 0.18\%$
300	3	$1.33 \pm 0.02\%$	$1.41 \pm 0.15\%$	$0.89 \pm 0.35\%$	$1.10 \pm 0.12\%$
400	3	$1.20 \pm 0.02\%$	$1.28 \pm 0.10\%$	$0.67 \pm 0.26\%$	$1.10 \pm 0.12\%$
500	3	$1.19 \pm 0.03\%$	$1.22 \pm 0.06\%$	$0.53 \pm 0.21\%$	$1.10 \pm 0.12\%$
600	3	$1.16 \pm 0.02\%$	$1.18 \pm 0.04\%$	$0.44 \pm 0.17\%$	$1.10 \pm 0.12\%$

fective junction-forming region. Moreover, since the standard deviation associated with the geometry-independent term $\sqrt{\text{Var}(G_0)}$ remains constant, its relative standard deviation $\sqrt{\text{Var}(G_0)}/G_N$ decreases as the junction area increases. This finding indicates that increasing the junction width is an effective way to suppress variations in practical fabrication processes.

We further examine the effect of deposition angle. For this purpose, bilayer junctions with a width of 300 nm were fabricated at deposition angles of 17° and 30° . The samples fabricated at 30° exhibit a substantially lower normalized RMS variation of $1.15 \pm 0.03\%$ compared with $1.92 \pm 0.03\%$ for those fabricated at 17° , corresponding to an overall reduction by a factor of 1.67 ± 0.04 . This improvement, however, cannot be explained solely by the increase in junction area. The increase in junction area resulting from changing the deposition angle from 17° to 30° , estimated from the average R_N , is 2.02 ± 0.09 , which corresponds to a reduction factor of 1.42 ± 0.03 in the normalized RMS variation. Assuming the same junction area as that obtained with the 30° deposition but a deposition angle of 17° , the expected normalized RMS variation is $1.35 \pm 0.04\%$. The experimentally observed value at 30° ($1.15 \pm 0.03\%$) is significantly lower than this expectation, indicating an additional suppression of film-thickness-induced contributions to the critical-current variation due to the deposition angle, consistent with the geometric factor in Eq. (13). This deposition-angle dependence also helps distinguish the film-thickness-related contribution from possible short-range resist-thickness variations. A local resist-thickness fluctuation would not be expected to follow the geometric factor $f(\theta, N_L)$, whereas the observed additional suppression at 30° is consistent with the vanishing of the bilayer thickness-related factor.

Based on the preceding experiments and analyses, we found that employing a bilayer structure with a 30° deposition angle is effective for suppressing the contribution of film-thickness fluctuations, and that increasing the junction area is effective for reducing the variation originating from geometry-independent terms. Motivated by these findings, we fabricated

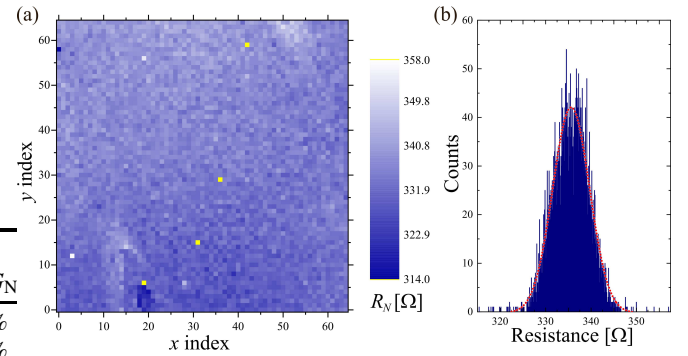


FIG. 3. Results of room-temperature resistance measurements for the 9.75 mm square junction array. (a) Two-dimensional map of the measured resistance. The four yellow points correspond to open or shorted junctions, which are excluded from the statistical analysis. (b) Histogram of the resistance values for all valid junctions. The red dashed line is a Gaussian curve shown as a guide to the eye.

and evaluated bilayer Josephson junctions using a 30° deposition angle, with the junction width set to 600 nm to further enhance uniformity.

Maintaining a uniform resist thickness is crucial in the Dolan-bridge process. To avoid the resist beads near the edge of the 17 mm square chip, the unit-cell size of the test junctions was reduced from $200 \mu\text{m}$ to $150 \mu\text{m}$, and junctions were fabricated within a 9.75 mm square region.

Figure 3 shows the results of the resistance measurements. The yield exceeded 99.9% [Fig. 3(a)]. As shown in Fig. 3(b), the histogram of the room-temperature resistance exhibits a nearly symmetric distribution, with a mean value of 335.5Ω , a standard deviation of 3.99Ω , and a relative standard deviation of 1.19% (4221 valid samples). This level of relative variation is comparable to the lowest values reported in the literature evaluating the variation of sparsely arrayed qubits in 10 mm square regions^{11,12}.

In addition, spatially correlated nonuniformities in the resistance are observed in the lower-left and upper-right regions of the chip [Fig. 3(a)], which are likely caused by resist-thickness undulations introduced during the spin-coating process. To evaluate the intrinsic uniformity without the influence of such artifacts, we performed a statistical analysis of the resistance values in smaller square regions that do not contain any open or shorted junctions and are unaffected by these resist-thickness undulations, as shown in Fig. 4(a). These regions were selected to minimize the contribution from long-range spatial nonuniformities. As shown in the histograms in Fig. 4(b)–(d), the distributions are nearly symmetric, and the relative standard deviations are 0.73% for the 4.5 mm square region with 961 junctions, 0.63% for the 3.0 mm square region with 441 junctions, and 0.50% for the 1.5 mm square region with 121 junctions. Because variations in resist thickness exhibit long correlation lengths, the relative standard deviation systematically decreases as the region size is reduced. This result indicates that, if a spatially uniform resist thickness can be achieved, the variation can potentially be suppressed to the level of 0.50%, as demonstrated in the 1.5 mm square re-

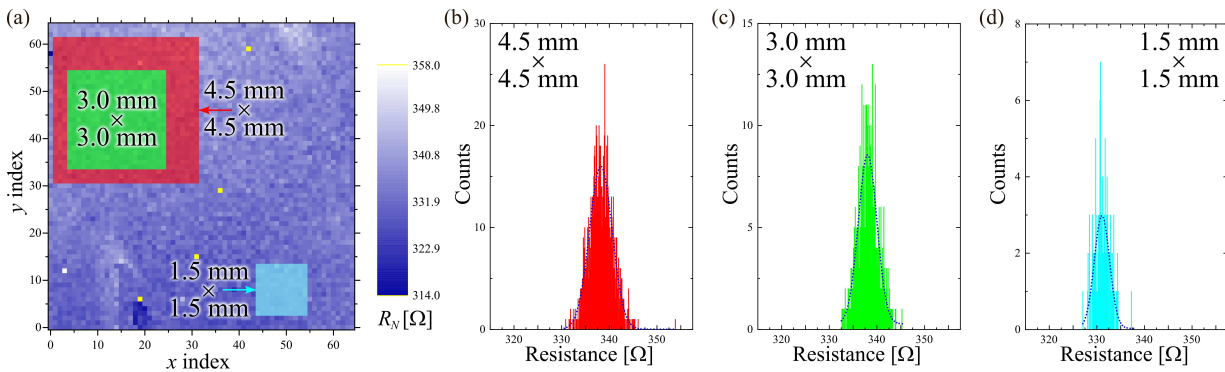


FIG. 4. (a) Schematic of three representative regions: 4.5 mm square (red), 3.0 mm square (green), and 1.5 mm square (cyan). The dataset is the same as that in Fig. 3. These regions are chosen to minimize standard deviations. (b–d) Corresponding histograms of the measured resistance values in these three regions. The dashed lines are Gaussian curves shown as guides to the eye.

gion.

In summary, the model-based analysis of the junction-geometry dependence revealed the origin of the critical-current variation in Dolan-bridge Josephson junctions. Among the modeled sources of variation, the film-thickness-related contribution was identified as the dominant component in the present dataset. Furthermore, the model suggests that a deposition angle of 30° for bilayer junctions minimizes the thickness-induced contribution, and this optimization was experimentally verified. The remaining long-range spatial nonuniformity observed over the chip is likely associated with resist-thickness variations introduced during the spin-coating process, which can be further mitigated through improved resist-coating procedures. This approach provides practical guidelines for scaling up superconducting quantum circuits based on Dolan-bridge Al/AIO_x/Al junctions. In addition, the model-based statistical framework developed in this work can be extended to quantify variations across different junction geometries and fabrication processes.

We also emphasize that the obtained level of uniformity is compatible with the requirements of large-scale integration of superconducting qubits, where variation in the critical current directly affects qubit frequency dispersion. By applying the same optimization to wafer-scale fabrication, the uniformity can be further improved, potentially reducing the calibration overhead of multi-qubit systems.

SUPPLEMENTARY MATERIAL

See the supplementary material for details of the derivation of Eq. (13).

AUTHOR DECLARATIONS

Conflict of interest

The authors have no conflicts to disclose.

DATA AVAILABILITY

The data that support the findings of this study are available from the corresponding author upon reasonable request.

- ¹G. J. Dolan, *Applied Physics Letters* **31**, 337 (1977).
- ²A. Potts, P. R. Routley, G. J. Parker, J. J. Baumberg, and P. A. J. de Groot, *Journal of Materials Science: Materials in Electronics* **12**, 289 (2001).
- ³M. V. Costache, G. Bridoux, I. Neumann, and S. O. Valenzuela, *Journal of Vacuum Science & Technology B* **30**, 04E105 (2012).
- ⁴Y. Nakamura, Y. A. Pashkin, and J. S. Tsai, *Nature* **398**, 786 (1999).
- ⁵J. Koch, T. M. Yu, J. Gambetta, A. A. Houck, D. I. Schuster, J. Majer, A. Blais, M. H. Devoret, S. M. Girvin, and R. J. Schoelkopf, *Phys. Rev. A* **76**, 042319 (2007).
- ⁶F. Arute, K. Arya, R. Babbush, D. Bacon, J. C. Bardin, R. Barends, R. Biswas, S. Boixo, F. G. S. L. Brandao, D. A. Buell, B. Burkett, Y. Chen, Z. Chen, B. Chiaro, R. Collins, W. Courtney, A. Dunsworth, E. Farhi, B. Foxen, A. Fowler, C. Gidney, M. Giustina, R. Graff, K. Guerin, S. Habegger, M. P. Harrigan, M. J. Hartmann, A. Ho, M. Hoffmann, T. Huang, T. S. Humble, S. V. Isakov, E. Jeffrey, Z. Jiang, D. Kafri, K. Kechedzhi, J. Kelly, P. V. Klimov, S. Knysh, A. Korotkov, F. Kostritsa, D. Landhuis, M. Lindmark, E. Lucero, D. Lyakh, S. Mandra, J. R. McClean, M. McEwen, A. Megrant, X. Mi, K. Michielsen, M. Mohseni, J. Mutus, O. Naaman, M. Neeley, C. Neill, M. Y. Niu, E. Ostby, A. Petukhov, J. C. Platt, C. Quintana, E. G. Rieffel, P. Roushan, N. C. Rubin, D. Sank, K. J. Satzinger, V. Smelyanskiy, K. J. Sung, M. D. Trevithick, A. Vainsencher, B. Villalonga, T. White, Z. J. Yao, P. Yeh, A. Zalcman, H. Neven, and J. M. Martinis, *Nature* **574**, 505 (2019).
- ⁷M. Brink, J. M. Chow, J. Hertzberg, E. Magesan, and S. Rosenblatt, in *2018 IEEE International Electron Devices Meeting (IEDM)* (2018) pp. 6.1.1–6.1.3.
- ⁸T. C. White, J. Y. Mutus, I.-C. Hoi, R. Barends, B. Campbell, Y. Chen, Z. Chen, B. Chiaro, A. Dunsworth, E. Jeffrey, J. Kelly, A. Megrant, C. Neill, P. J. J. O’Malley, P. Roushan, D. Sank, A. Vainsencher, J. Wenner, S. Chaudhuri, J. Gao, and J. M. Martinis, *Applied Physics Letters* **106**, 242601 (2015).
- ⁹C. Macklin, K. O’Brien, D. Hover, M. E. Schwartz, V. Bolkhovskiy, X. Zhang, W. D. Oliver, and I. Siddiqi, *Science* **350**, 307 (2015).
- ¹⁰S. Ó Peatáin, T. Dixon, P. J. Meeson, J. M. Williams, S. Kafanov, and Y. A. Pashkin, *Superconductor Science and Technology* **36**, 045017 (2023).
- ¹¹J. M. Kreikebaum, K. P. O’Brien, A. Morvan, and I. Siddiqi, *Superconductor Science and Technology* **33**, 06LT02 (2020).
- ¹²T. Takahashi, N. Kouma, Y. Doi, S. Sato, S. Tamate, and Y. Nakamura, *Japanese Journal of Applied Physics* **62**, SC1002 (2022).
- ¹³D. O. Moskalev, E. V. Zikiy, A. A. Pishchimova, D. A. Ezenkova, N. S. Smirnov, A. I. Ivanov, N. D. Korshakov, and I. A. Rodionov, *Scientific Reports* **13**, 4174 (2023).

¹⁴A. A. Pishchimova, N. S. Smirnov, D. A. Ezenkova, E. A. Krivko, E. V. Zikiy, D. O. Moskalev, A. I. Ivanov, N. D. Korshakov, and I. A. Rodionov, *Scientific Reports* **13**, 6772 (2023).

¹⁵Y. Zheng, S. Li, Z. Ding, K. Xiong, J. Feng, and H. Yang, *Scientific Reports* **13**, 11874 (2023).

¹⁶V. Ambegaokar and A. Baratoff, *Phys. Rev. Lett.* **10**, 486 (1963).

Supplementary Material

Geometric dependence of critical-current variation in Al/AIO_x/Al Josephson junctions: a model-based analysis

I. DERIVATION OF THE GEOMETRIC FACTOR $f^2(\theta, N_L)$ IN EQ. (13)

This section derives the geometric factor $f^2(\theta, N_L)$ introduced in Eq. (13) of the main text. We consider a Dolan-bridge double-angle deposition with angles $\pm\theta$ (Fig. 1(a) in the main text). Let H be the vertical distance between the substrate plane and the intersection point of the two evaporation-beam center lines (a resist-geometry-dependent height parameter). The thickness of the n -th deposited Al layer is denoted by d_n ($n = 1, \dots, N_L$), and the junction width is W .

A. Junction-interface area formed between layers n and $n+1$

In this geometry, the junction interface between the n -th and $(n+1)$ -th layers consists of two contributions (see Fig. 1(a), right panel): (i) the top-surface overlap and (ii) the sidewall-surface overlap.

After depositing the first n layers, the effective vertical level relevant to the top overlap is shifted by $\sum_{k=1}^n d_k$. The top-overlap length (projected in the lateral direction) is therefore

$$\ell_n = 2 \tan \theta \left(H - \sum_{k=1}^n d_k \right). \quad (\text{S1})$$

The sidewall-overlap length associated with the n -th layer is

$$s_n = \frac{d_n}{\cos \theta}. \quad (\text{S2})$$

Thus, the junction-interface area created between layers n and $n+1$ is

$$S_{n,n+1} = W(\ell_n + s_n) = W \left[2 \tan \theta \left(H - \sum_{k=1}^n d_k \right) + \frac{d_n}{\cos \theta} \right]. \quad (\text{S3})$$

For an N_L -layer junction, the total junction-interface area is the sum over $n = 1, \dots, N_L - 1$:

$$S_{N_L} = \sum_{n=1}^{N_L-1} S_{n,n+1}. \quad (\text{S4})$$

B. Area fluctuation induced by thickness fluctuations

We consider small thickness fluctuations $d_n \rightarrow d_n + \delta d_n$ and compute the induced area fluctuation

$$\delta S_{N_L} = \sum_{i=1}^{N_L-1} \frac{\partial S_{N_L}}{\partial d_i} \delta d_i. \quad (\text{S5})$$

From the expression for $S_{n,n+1}$, the derivative with respect to d_i receives (i) a positive sidewall contribution from s_i and (ii) negative top-overlap contributions because d_i appears in ℓ_n for all $n \geq i$. A straightforward differentiation yields

$$\begin{aligned} \frac{\partial S_{N_L}}{\partial d_i} &= W \left[\frac{1}{\cos \theta} - \sum_{n=i}^{N_L-1} 2 \tan \theta \right] \\ &= W \left[\frac{1}{\cos \theta} - 2(N_L - i) \tan \theta \right] \\ &= \frac{W}{\cos \theta} [1 - 2(N_L - i) \sin \theta]. \end{aligned} \quad (\text{S6})$$

C. Variance and closed-form expression

Assuming that thickness fluctuations of different layers are uncorrelated and have the same variance,

$$\langle \delta d_i \delta d_j \rangle = \delta_{ij} \langle (\delta d)^2 \rangle, \quad (\text{S7})$$

we obtain

$$\langle (\delta S_{N_L})^2 \rangle = \sum_{i=1}^{N_L-1} \left(\frac{\partial S_{N_L}}{\partial d_i} \right)^2 \langle (\delta d)^2 \rangle. \quad (\text{S8})$$

Using Eq. (S6),

$$\left(\frac{\partial S_{N_L}}{\partial d_i} \right)^2 = \frac{W^2}{\cos^2 \theta} [1 - 2(N_L - i) \sin \theta]^2. \quad (\text{S9})$$

In the main text, the thickness-induced variance contribution is written as

$$\text{Var}(G_d) = c_d f^2(\theta, N_L) W^2, \quad (\text{S10})$$

where $f^2(\theta, N_L)$ is defined (up to the proportionality constant absorbed into c_d) by

$$f^2(\theta, N_L) = \frac{1}{W^2} \sum_{i=1}^{N_L-1} \left(\frac{\partial S_{N_L}}{\partial d_i} \right)^2 = \frac{1}{\cos^2 \theta} \sum_{i=1}^{N_L-1} [1 - 2(N_L - i) \sin \theta]^2. \quad (\text{S11})$$

Let $m = N_L - i$ so that $m = 1, 2, \dots, N_L - 1$. Then

$$f^2(\theta, N_L) = \frac{1}{\cos^2 \theta} \sum_{m=1}^{N_L-1} (1 - 2m \sin \theta)^2 = \frac{1}{\cos^2 \theta} \sum_{m=1}^{N_L-1} (1 - 4m \sin \theta + 4m^2 \sin^2 \theta). \quad (\text{S12})$$

Using

$$\sum_{m=1}^{N_L-1} 1 = N_L - 1, \quad \sum_{m=1}^{N_L-1} m = \frac{(N_L - 1)N_L}{2}, \quad \sum_{m=1}^{N_L-1} m^2 = \frac{(N_L - 1)N_L(2N_L - 1)}{6}, \quad (\text{S13})$$

we obtain the closed form

$$\begin{aligned} f^2(\theta, N_L) &= \frac{N_L - 1}{\cos^2 \theta} \left[1 - 2N_L \sin \theta + \frac{2N_L(2N_L - 1)}{3} \sin^2 \theta \right] \\ &= \frac{N_L - 1}{\cos^2 \theta} \left[2N_L \sin \theta \left(\frac{2N_L - 1}{3} \sin \theta - 1 \right) + 1 \right], \end{aligned} \quad (\text{S14})$$

which reproduces Eq. (13) in the main text.

D. Special case: bilayer junction ($N_L = 2$)

For $N_L = 2$, the above expression reduces to

$$f^2(\theta, 2) = \frac{1}{\cos^2 \theta} (1 - 2 \sin \theta)^2 = \left(\frac{1}{\cos \theta} - 2 \tan \theta \right)^2, \quad (\text{S15})$$

which corresponds to Eq. (14) in the main text.